OAK RIDGE
NATIONAL LABORATORY
MANAGED BY UT-BATTELLE
FOR THE DEPARTMENT OF ENERGY

ORNL/TM-2010/346

Assessment of Initial Test Conditions for Experiments to Assess Irradiation Assisted Stress Corrosion Cracking Mechanisms

December 2010

Prepared by

J.T. Busby and M.N. Gussev
Oak Ridge National Laboratory

UT-BATTELLE
ORNL-27 (4-00)

ORNL/TM-2010/346

Light Water Reactor Sustainability

Assessment of Initial Test Conditions for Experiments to Assess Irradiation Assisted Stress Corrosion Cracking Mechanisms

J.T. Busby and M.N. Gussev
Materials Science and Technology Division
Oak Ridge National Laboratory

Date Published: December 2010

Prepared under the direction of the
U.S. Department of Energy
Office of Nuclear Energy
Light Water Reactor Sustainability
Materials Aging and Degradation Pathway

Prepared by
OAK RIDGE NATIONAL LABORATORY
Oak Ridge, Tennessee 37831-6283
managed by
UT-BATTELLE, LLC
for the
U.S. DEPARTMENT OF ENERGY
under contract DE-AC05-00OR22725

This page intentionally left blank

CONTENTS

Page

This page intentionally left blank

LIST OF FIGURES

Figure **Page**

This page intentionally left blank

LIST OF TABLES

This page intentionally left blank

ACKNOWLEDGMENTS

This research was sponsored by the U.S. Department of Energy, Office of Nuclear Energy, for the Light Water Reactor Sustainability Research and Development effort. The authors are also appreciative to Drs. T.M. Rosseel and L. Tan for their input and suggestions.

This page intentionally left blank

EXECUTIVE SUMMARY

Irradiation-assisted stress corrosion cracking is a key materials degradation issue in today's nuclear power reactor fleet and affects critical structural components within the reactor core. The effects of increased exposure to irradiation, stress, and/or coolant can substantially increase susceptibility to stress-corrosion cracking of austenitic steels in high-temperature water environments. Despite 30 years of experience, the underlying mechanisms of Irradiation Assisted Stress Corrosion Cracking (IASCC) are unknown. Extended service conditions will increase the exposure to irradiation, stress, and corrosive environments for all core internal components. The objective of this effort within the Light Water Reactor Sustainability (LWRS) program is to evaluate the response and mechanisms of IASCC in austenitic stainless steels with single variable experiments.

A group of high-value irradiated specimens has been acquired from international research programs, providing a valuable opportunity to examine the mechanisms of IASCC. This batch of irradiated specimens has been received and inventoried. In addition, visual examination and sample cleaning has been completed.

Microhardness testing has been performed on these specimens. All samples show evidence of hardening, as expected, although the degree of hardening has saturated and no trend with dose is observed. Further, the change in hardening can be converted to changes in mechanical properties. The calculated yield stress is consistent with previous data from light water reactor conditions.

In addition, some evidence of changes in deformation mode was identified via examination of the microhardness indents. This analysis may provide further insights into the deformation mode under larger scale tests.

Finally, swelling analysis was performed using immersion density methods. Most alloys showed some evidence of swelling, consistent with the expected trends for this class of alloy. The Hf-doped alloy showed densification rather than swelling. This observation may be related to the formation of second-phases under irradiation, although further examination is required.

This page intentionally left blank

1. INTRODUCTION

Nuclear power currently provides a significant fraction of the United States' non-carbon emitting power generation. In future years, nuclear power must continue to generate a significant portion of the nation's electricity to meet the growing electricity demand, clean energy goals, and ensure energy independence. New reactors will be an essential part of the expansion of nuclear power. However, given limits on new builds imposed by economics and industrial capacity, the extended service of the existing fleet will also be required.

Ensuring public safety and environmental protection is a prerequisite to all nuclear power plant operating and licensing decisions at all stages of reactor life. This includes the original license period of 40 years, the first license extension to 60 years, and certainly for any consideration of life beyond 60 years. For extended operating periods, it must be shown that adequate aging management programs are present or planned and that appropriate safety margins exist throughout the subsequent license renewal periods. Materials degradation can impact reactor reliability, availability, and potentially, safe operation. Components within a reactor must tolerate the harsh environment of high temperature water, stress, vibration, and/or an intense neutron field. Degradation of materials in this environment can lead to reduced performance, and in some cases, sudden failure. Clearly, understanding materials degradation and accounting for the effects of a reactor environment in operating and regulatory limits is essential.

The Light Water Reactor Sustainability (LWRS) Program is designed to support the long-term operation (LTO) of existing domestic nuclear power generation with targeted collaborative research programs into areas beyond current short-term optimization opportunities [1]. Within the LWRS program, four pathways have been initiated to perform research essential to informing relicensing decisions [1]. The Materials Aging and Degradation Pathway is designed to help develop the scientific basis for understanding and predicting long-term environmental degradation behavior of materials in nuclear power plants and to provide data and methods to assess performance of systems, structures, and components essential to safe and sustained operation.

The effects of irradiation can substantially increase susceptibility to stress-corrosion cracking of austenitic steels in high-temperature water environments. This form of degradation, termed irradiation-assisted stress-corrosion cracking (IASCC), has been observed in both boiling water reactors (BWRs) and pressurized water reactors (PWRs), although higher irradiation doses are required for the onset of IASCC in PWRs. Both 304 and 316 stainless steel are susceptible to this form of degradation. For regulators and industry, IASCC is a key materials degradation issue in today's nuclear power reactor fleet and affects critical structural components within the reactor core. With additional exposure to the combined effects of coolant, stress, and irradiation under extended service, this form of degradation is expected to grow more severe and additional materials may become susceptible. Despite 30 years of experience, the underlying mechanisms of IASCC are unknown.

The objective of this work is to evaluate the response and mechanisms of IASCC in austenitic stainless steels with single variable experiments. Crack growth rate tests and complementary microstructure analysis will provide a more complete understanding of IASCC by building on past Electrical Power Research Institute (EPRI)-led work for the Cooperative IASCC Research Group. Experimental research will include crack-growth testing on high-fluence specimens of single-variable alloys in simulated LWR environments, tensile testing, hardness testing, microstructural and microchemical analysis, and detailed efforts to characterize localized deformation. This is a collaborative research effort lead by the University of Michigan with Oak Ridge National Laboratory and Pacific Northwest National Laboratory providing support. A detailed description of the larger

effort, sample matrix, and single-variable experiment plan is given in Ref. [2].

In this report, the characterization of an initial set of test specimens is provided. This analysis includes hardness testing, deformation evaluation and an estimation of swelling. These complementary bits of analysis provide key information that, when combined with the mechanical testing performed in simulated LWR environments, will provide better understanding of the driving forces for IASCC and help identify mitigation strategies.

2. TEST MATERIALS

As noted in Ref. [2], this effort builds heavily on past research and programs conducted by the Cooperative IASCC Research (CIR) programs. The objective of the CIR program was to help develop predictive models and mitigations strategies for IASCC. Progress in the CIR program included a detailed-white paper review on IASCC subjects and a systematic and detailed characterization of irradiation-induced microstructure and cracking response in stainless steels (from both neutron and proton-irradiations).

2.1 ALLOY AND SAMPLE DESCRIPTION

In addition, the CIR program also conducted an irradiation campaign in the BOR-60 reactor including a series of 20 single-variable alloys with different compositions and thermo-mechanical states. The alloys are described in Table 1. The CIR program concluded crack-growth testing on a number of these irradiated conditions. That effort provides a solid foundation for the LWRS program.

Table 1: Chemical composition of CIR alloys (compositions in at %)

Alloy	Note	C	Mn	Si	P	S	Cr	Ni	Mo	N	Nb	Ti	O	Co	Cu	Hf
A	Commercial	0.023	1.82	0.56	0.023	0.015	19.95	10.8	0.53	0.072	<0.001	0.02	0.011	0.22	0.29	
B	Commercial	0.056	1.13	0.73	0.022	0.022	16.84	10.54	2.25	0.021	0.008	0.01	0.009	0.12	0.25	
C	Commercial	0.07	1.4	0.56	0.013	0.007	16.77	12.78	2.18	0.008	<0.01	0.38	0.004	0.1	0.06	
SW	Swedish commercial	0.022	1.07	0.24	0.015	<0.002	18.42	10.45	-	0.025	-	-	-	-	-	
E	HP	0.021	0.94	0.04	<0.01	0.003	18.76	12.37	0.04	0.0003	0.005	0.01	0.004	0.01	<0.01	
F	HP	0.008	0.98	0.03	<0.01	0.003	18.17	12.06	0.02	0.0005	0.002	0.01	0.013	0.01	<0.01	
G	HP	0.02	0.97	0.03	<0.01	0.002	18.26	12.15	2.36	0.0004	0.003	0.01	0.005	0.01	0.01	
H	HP	0.02	1.01	1.05	<0.01	0.002	18.17	12.45	0.02	0.0005	<0.001	0.01	0.007	0.01	<0.01	
I	HP	0.007	1.01	0.03	0.016	0.003	18.21	12.11	0.02	0.0004	<0.001	0.01	0.012	0.01	<0.01	
K	HP	0.02	1	0.03	<0.01	0.002	18.21	25.08	0.02	0.0005	<0.001	0.01	0.003	0.01	<0.01	
L	HP	0.02	1.02	0.03	<0.01	0.002	25.22	25.07	0.02	0.0005	<0.001	0.01	0.009	0.01	0.01	
M	HP	0.02	1	0.03	<0.01	0.003	18.03	11.22	0.02	0.0005	<0.001	0.3	0.011	0.73	<0.01	
N	HP	0.02	1	0.03	<0.01	0.003	18.24	12.12	0.02	0.0004	0.595	0.01	0.004	0.01	<0.01	
P	HP	0.028	1.01	0.1	0.01	0.007	17.03	13.6	2.18							1.17

In addition to the wealth of previous data, the CIR program also had a series of key untested specimens. The LWRS program has acquired these samples and preliminary characterization has been completed as noted in a section below. The crack-growth specimen conditions and tensile specimen conditions are shown in Tables 2 and 3, respectively. More details on each of the specimen conditions are given in [2].

Table 2: Inventory of compact tension specimens for this effort

Specimen No.	CG-BS01	CG-GS01	CG-IP01	CG-MS01	CG-NS01	CG-PS02
Heat Serial	BS	GS	IP	MS	NS	PS
Material	316	304	304 (SA 304L)	304	304	316L
Material Type	SA, Baffle Bolt	HP	HP	HP	HP	HP
Solute Additions	None	Mo	- C, P	Ti	Nb	Hf
Dose, dpa	5.5	11.8	4.4	10.7	10.7	9.6
Reactor	Boris 6	Boris 6	Boris 7	Boris 7	Boris 7	Boris 7
Date of Out the Reactor	Oct. 2001	Oct. 2002	June, 2004	June, 2004	June, 2004	Oct. 2003
Specimen Type	RCT	RCT	RCT	RCT	RCT	RCT
Specimen Thickness	8 mm	6 mm	8 mm	8 mm	8 mm	8 mm

Table 3: Inventory of tensile specimens for this effort

No.	Specimen	Material	Material Type	Heat Serial	Solute Additions	Reactor	Date out of reactor	Dose, dpa
1	AS13	304L	SA, Shroud	AS	None	Boris 6	Oct., 2001	5.5
2	AS14	304L	SA, Shroud	AS	None	Boris 6	Oct., 2001	5.5
3	AS17	304L	SA, Shroud	AS	None	Boris 6	Oct., 2002	10.2
4	AS18	304L	SA, Shroud	AS	None	Boris 6	Oct., 2002	10.2
5	AS19	304L	SA, Shroud	AS	None	Boris 6	Oct., 2002	10.2
6	BS13	316	SA, Bolt	BS	None	Boris 6	Oct., 2001	5.5
7	BS16	316	SA, Bolt	BS	None	Boris 6	Oct., 2002	10.2
8	BR15	316	CW, Bolt	BR	None	Boris 6	Mar., 2003	4.8
9	B124(2)	316	CW, Bolt	B	None	Boris 6	Mar., 2003	25
10	B125(3)	316	CW, Bolt	B	None	Boris 6	Mar., 2003	25
11	B126	316	CW, Bolt	B	None	Boris 6	Mar., 2003	25
12	CR13	316	CW, Ti St.	CR	Ti	Boris 6	Mar., 2003	4.8
13	CR14	316	CW, Ti St.	CR	Ti	Boris 6	Mar., 2003	4.8
14	(CR17)	316	CW, Ti St.	CR	Ti	Boris 6	Mar., 2003	25
15	(CR18)	316	CW, Ti St.	CR	Ti	Boris 6	Mar., 2003	25
16	CR19	316	CW, Ti St.	CR	Ti	Boris 6	Mar., 2003	25
17	ES13	304	HP	ES	None	Boris 6	Oct., 2002	11.8
18	ES14	304	HP	ES	None	Boris 6	Oct., 2002	11.8
19	ES16	304	HP	ES	None	Boris 6	Oct., 2002	10.2
20	GS13	304	HP	GS	Mo	Boris 6	Oct., 2002	11.8
21	GS14	304	HP	GS	Mo	Boris 6	Oct., 2002	11.8
22	AS22	304L	SA, Shroud	AS	None	Boris 7	June, 2004	47.5
23	AS23	304L	SA, Shroud	AS	None	Boris 7	June, 2004	47.5
24	BS18	316	SA, Bolt	BS	None	Boris 7	June, 2004	47.5
25	ES21	304	HP	ES	None	Boris 7	June, 2004	10.7
26	LS13	304	HP	LS	Cr, Ni	Boris 7	Oct., 2003	9.1
27	FS13	304	HP	FS	- C	Boris 7	Oct., 2003	9.1
28	HS13	304	HP	HS	Si	Boris 7	Oct., 2003	7.8
29	KS13	304	HP	KS	Ni	Boris 7	Oct., 2003	9.6
30	PS13	304	HP	PS	Hf	Boris 7	Oct., 2003	9.6
31	PS14	304	HP	PS	Hf	Boris 7	Oct., 2003	9.6
32	PS15	304	HP	PS	Hf	Boris 7	Oct., 2003	9.6
33	SW36	304L	SA, Swedish	SW	None	Boris 7	June, 2004	4.4
34	SW37	304L	SA, Swedish	SW	None	Boris 7	June, 2004	4.4

* CR17 and CR18 are missing; B122 and B123 are available.

2.2 PRELIMINARY CHARACTERIZATION

In late July 2010, a shipment of radioactive specimens was received at ORNL from Studsvik. A total of 33 specimens were part of that shipment, including 27 tensile specimens and 6 compact tensile specimens. Initial characterization and testing has included several key steps. First, samples were inventoried and inspected. Dose rates were measured. A subset of samples has been transferred from the ORNL Irradiated Materials Examination and Testing (IMET) hot cell to a low radioactive facility. Further specimen characterization has been performed. These initial steps are described in the sections below.

2.2.1. Sample identification

As noted above, a total of 33 specimens were received at the IMET hot cell facility. All expected specimens were accounted for, including 27 tensile specimens and 6 compact tension specimens. All

specimens were positively identified by a series of engraved identification numbers. An example is shown in Figure 1.

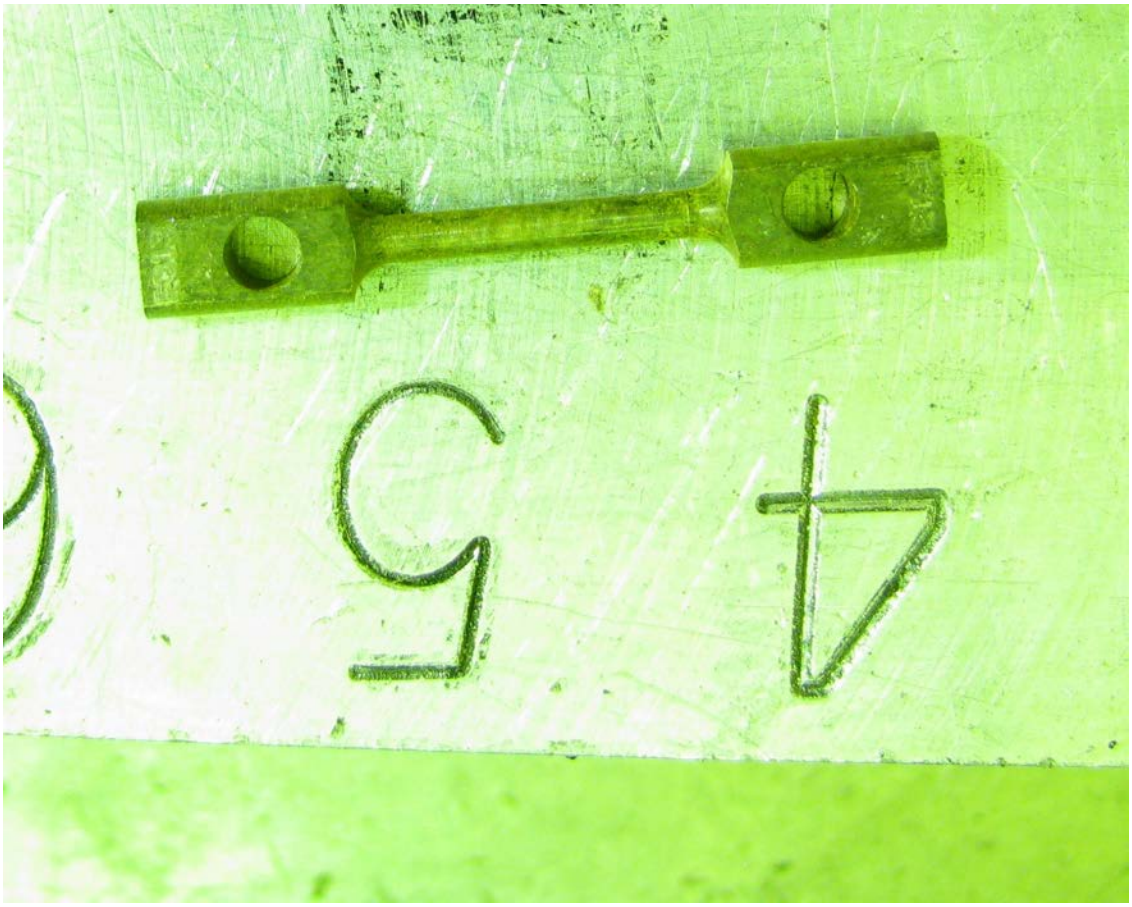

Figure 1: Sample BS13

2.2.2. Dose rate measurement

Dose rate measurements have been taken for all 33 specimens. The results are shown in Table 4 for each specimen. The dose rates are lower than expected for stainless steel specimens irradiated to high fluence, but this enables other testing options.

Table 4: Summary of dose rate measurements on specimens.

Sample ID	Sample Type	Dose rate (mR/hr at 30 cm)
BS01	1 CT	80
GS01	1 CT	30
IP01	1 CT	60
MS01	1 CT	130
NS01	1 CT	140
PS02	1 CT	100
AS13	TENSILE	19
AS14	TENSILE	18
AS17	TENSILE	38
AS18	TENSILE	38
AS19	TENSILE	34
AS22	TENSILE	150
AS23	TENSILE	150
B122	TENSILE	14
B123	TENSILE	14
BR15	TENSILE	12
BS13	TENSILE	11
BS16	TENSILE	20
BS18	TENSILE	9
CR13	TENSILE	13
CR14	TENSILE	10
ES13	TENSILE	35
ES14	TENSILE	9
ES16	TENSILE	7
ES21	TENSILE	15
FS13	TENSILE	107
GS13	TENSILE	9
GS14	TENSILE	9
HS13	TENSILE	300
KS13	TENSILE	16
PS13	TENSILE	14
PS14	TENSILE	12
PS15	TENSILE	13

2.2.3. Further sample characterization

The lower dose rates (<60 mR/hr at 30 cm) for the tensile specimens permits additional options in sample characterization and analysis since non-hot cell facilities can be utilized. In particular, the Low Activation Materials Design and Analysis (LAMDA) laboratories at ORNL are ideal for such work. In late August, the first 8 tensile specimens were transferred to the LAMDA facility from the IMET. An additional characterization has been performed to assess sample polishing and cleaning needs.

The first batch of specimens, including BS13, BS16, BS18, ES14, ES21, GS14, PS15, and B123 were examined in September. It was important to estimate samples conditions, find any damage and

unexpected peculiarities, and define further steps. Samples are shown in Figure 2.

Figure 2: General view of subset of tensile samples

All samples were found to have an oxide layer with color varying from gray or metallic to dark blue and black, which will require electro-polishing prior to density and electro-resistivity measurement.

Further, all samples have gauge sections with light traces (steps of ~100-200 μm, and gouges ~20-50 μm) from a cutting tool. Before mechanical testing is performed, preliminary mechanical polishing and electro-chemical polishing will be required. Also flat surfaces of samples' head (for all samples) need to be polished prior to microhardness measurements. No any serious damage (bend, traces of blows, deep scratches) was found.

Three kinds of unexpected defects were found.

- Samples PS15 and BS18 have small holes for sample fixture (see Figure 3). This can lead to additional problems during mechanical testing, but there is also an advantage: more space is available for indentation. If possible, any additional drilling of these samples should be avoided.
- End faces of many samples have holes of different depth (from 0.1 to 1-1.5 mm). After electro polishing, checking these holes for contamination by oxides etc., is required.
- There are undocumented marks on the heads of some samples (see Figure 4). Since it is very coarse and deep (indents of numbering tool), it is unlikely that these heads can be used for ball indentation. They may, however, be available for annealing experiments.

Another anomaly is the size of loading hole and variation in that dimension as shown in Figure 3. In the case of high deformation hardening and increasing loads these locations could be involved in severe deformation. Prior to testing, this issue must be carefully evaluated using experiments on unirradiated samples with comparable level of strength.

Figure 3: Sample with small fixture hole (at the left) comparing to the normal (expected) hole diameter.

Figure 4: Deep coarse numbering: the coarse number of specimen (at the left) and unexpected undocumented characters (at the right).

3. HARDNESS TESTING

The direct measurement of yield strength of irradiated materials is the most desirable way to monitor irradiation-induced hardening. However, the handling and testing of samples with high residual radioactivity is more difficult as the testing must be performed in hot cells. As such, the yield stress of a neutron-irradiated alloy can be difficult to determine when compared to unirradiated materials. Correlations have been developed which allow calculation of expected yield strengths from measured microstructural features such as dislocation loops and voids. However, the existing database of radiation-induced microstructure is also relatively sparse and the correlations are not yet widely developed for all alloys of interest.

Microhardness testing provides an alternative means of assessing changes in mechanical properties. Vickers hardness testing can be done quickly and efficiently, without need for a large volume of sample material; an important consideration for highly radioactive neutron-irradiated materials. Microhardness testing is also quasi-non-destructive leaving much of the sample available for other tests.

In this effort, microhardness has been utilized to provide an initial estimate of hardening on the ends of the tensile bars. This data will help provide complementary data to the mechanical testing that will be performed in water. Initially, this testing has been performed on eight specimens that will comprise the first two tensile tests in water.

3.1. MICROHARDNESS PROCEDURES

Hardness was measured on irradiated tensile specimens of each alloy and on unirradiated materials where available. Hardness measurements were performed using a Wilson Instruments hardness indenter equipped with a Vickers indenter tip. All indents were made on the end regions of the specimen, well away from the gage length so that later tensile tests are not influenced.

Indentations were performed with a Vickers indenter tip using a 0.1, 0.2, and 0.5 kg load. The dwell time was set at 15 seconds for all indents. Nominally, at least five indents were taken on each specimen. Before measurement of irradiated samples, the calibration and accuracy of the microhardness device was checked with help of 2 etalon calibration samples with known microhardness values. The check of accuracy was conducted at the beginning and end of each day of testing. In all cases, the difference between the etalon specimens' nominal microhardness and the device readings did not exceed 2%. An average deviation was about 1.5%, within the expected range of deviation for the calibration samples.

All irradiated samples were electropolished prior to the microhardness measurements. Surface quality was sufficient in all cases as there were no rough scratches, dirt or contamination. In some cases, very light scratches caused by handling were found (see Figure 5). Unscratched areas were selected for indentation if possible. In all cases, the distance between indentations was more than 2.5 times the diagonal size as recommended by the ASTM E384 standard. However, ASTM E384 also recommends using a load value high enough to achieve indentation size about 50% of the viewing area. For this work, it was impossible because of the high strength of materials under investigation. Even if a 500g load was used, the indentation size did not exceed ~30% of visible screen area.

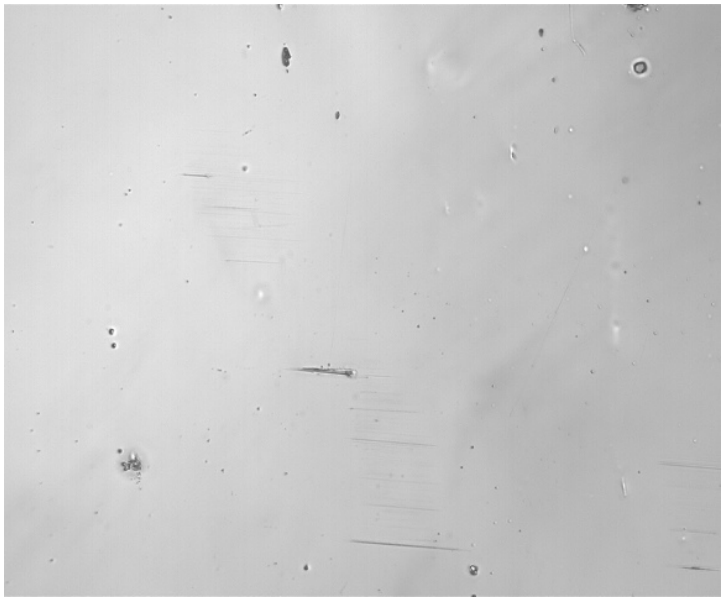

Figure 5: Sample B123 surface (one of samples' heads). A clear surface with some insignificant amount of carbides and other inclusions is observed. Very light scratches are also visible. Sample handling caused the minor scratches on the heads.

3.2. HARDNESS RESULTS

As noted above, three different loads were used during measurements: 100, 200 and 500 g. The different loads provide several key advantages. Firstly, the use of different loads provides the ability to check the present of surface deformation. In addition, different loads allow for the investigation of irradiated material deformation peculiarities around indentation, as will be discussed in a later section. The results of microhardness measurements are given in Table 5. In all cases, the microhardness data is an average value of 5 or more independent measurements (except BS16 for which 3 indentations were performed for each load value).

Table 5:Microhardness values for initial batch of tensile specimens.

Sample code	Material	Dose, dpa	load 100 g.	load 200g	load 500g
ES21	HP304 SS	10.7	361	358	356
B123	CW316	25	415	393	398
BS13	SA316*	5.5	467	467	453
BS16	SA316*	10.2	489	469	481
ES14	HP304L	11.8	364	364	348
GS14	HP304+Mo	11.8	371	352	350
HS13	HP304+Si	7.8	388	372	363
PS15	HP304+Hf	9.6	337	331	326

* Possibly, these samples were not annealed, but were cold worked.

Most data points are in a range of 300-400 kg/cm2, which is typical for highly irradiated stainless steels. However, there are 2 exceptions to this data range. Samples: BS13 and BS16 samples, microhardness values for these samples are significantly above 400 kg/cm2.

When sample BS16 registered a value of 500 kg/cm2 for, the measurement was interrupted, the irradiated sample was removed, and the microhardness device re-checked with etalon samples, which demonstrated that the device was fully functional. The BS 16 measurement was repeated with only3 indentations per load instead of 5. This is the data shown in the table above. The same procedure (irradiated sample removal, checking with control sample or both, re-measurement of irradiated sample) was executed for BS13 (microhardness above 450) and PS15 (microhardness significantly below 350, the softest sample).

Upon further evaluation, it was determined that the BS sample condition was not in the solution annealed state. Rather, all the BS specimens in the CIR program were irradiated in the cold-worked condition (approximately 20% cold-worked). Taking into consideration the different starting conditions, the higher hardness levels for samples BS13 and BS16 is reasonable.

Figure 6 shows microhardness value as function of load. One should note there are no critical differences between microhardness values for smallest (100g) and highest (500g) loads. Typically, the difference does not exceed 3-5% between the loads indicating the quality of surface is sufficient and that there is no cold work on the surface or any other anomaly.

One can also note that the microhardness value decreases with increasing load and reaches a "saturated" value. This phenomenon is well known for un-irradiated metals and alloys, but for accurate measurement of the influence of radiation, one needs to measure the same material before irradiation. It is interesting to investigate the "load factor" for highly irradiated steels because of the propensity for irradiated material to undergo localized deformation localization (e.g. the formation of defect-free channels).

Data were also taken from unirradiated samples provided by the University of Michigan using the same procedures discussed above. Not all conditions were available (notably for B and BS conditions). In these cases, unirradiated hardness data were taken from the previous CIR program. The irradiated and unirradiated data are shown together in Table 6 for 500 g loads.

The hardness data can be used to estimate the change in yield strength using a relation developed by Busby et al. [3]. While there are several possible routes to estimate yield strength from hardness, the most straightforward is given as:

$$\Delta\sigma_y = 3.03\,\Delta H_V,$$

where $\Delta\sigma_y$ is expressed in MPa and ΔH_v is expressed in kg/mm^2.

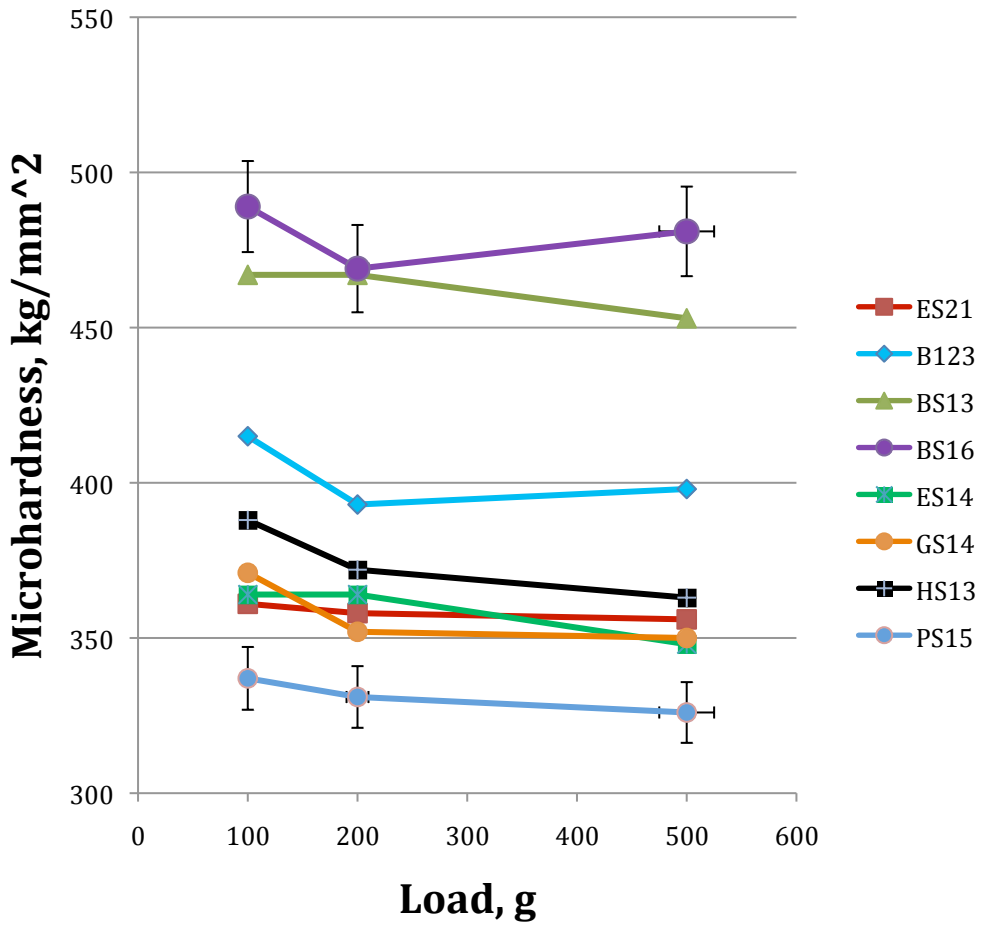

Figure 6: Microhardness value as function of load. For most soft and hard specimens the 3% error bars are shown.

Table 6:Microhardness values for initial batch of tensile specimens (500 g load).

Sample code	Material	Dose, dpa	Irradiated Hardness (kg/mm2)	Unirradiated Hardness (kg/mm2)	Change in Hardness (kg/mm2)	Change in Yield Stress (MPa)
ES21	HP304 SS	10.7	361	119	242	733
B123	CW316	25	415	205*	210	636
BS13	SA316*	5.5	467	348*	119	361
BS16	SA316*	10.2	489	348*	141	427
ES14	HP304L	11.8	364	119	245	742
GS14	HP304+Mo	11.8	371	121	250	758
HS13	HP304+Si	7.8	388	141	247	748
PS15	HP304+Hf	9.6	337	125	212	642

*Data taken from previous CIR study

3.3. COMPARISON WITH PAST STUDIES

The results in Table 6 can readily be compared with data in the literature and values from past studies on these same materials. The calculated yield strength from the hardness data of this study are plotted versus measured yield strength from a variety of studies on 316 stainless steel in light water reactors. The data from this study (assuming an unirradiated yield stress of 220 MPa) are well in line with the expected trends and data from past studies. Further the observed saturation of hardness as a function of dose in this study is consistent with past observations.

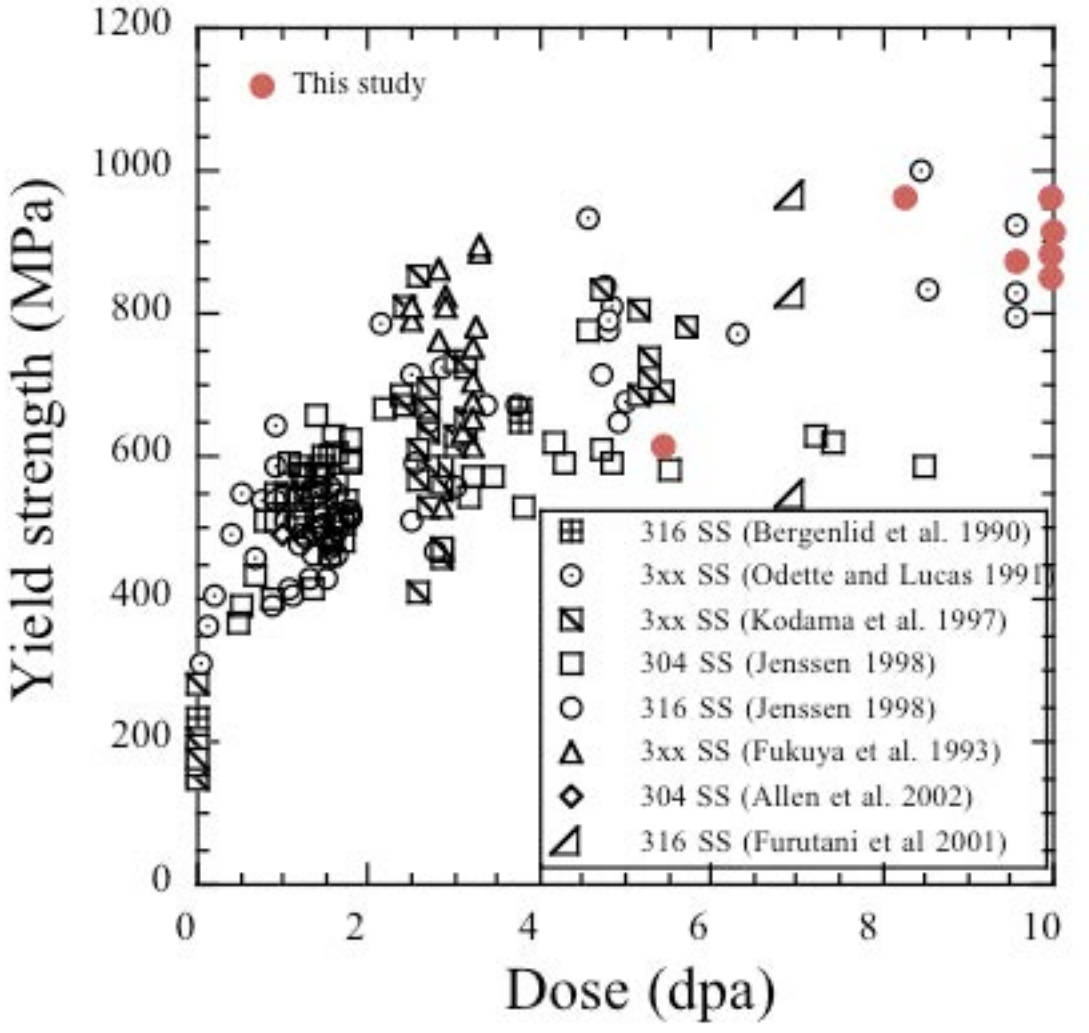

Figure 7: Comparison of irradiation hardening of this work with previous studies on 316 stainless steel in light water reactors.

4. ANALYSIS OF DEFORMATION AROUND HARDNESS INDENTATIONS

Microscopic investigation of the indentation structure found that the pyramid indentation during microhardness measurement leads to the formation of complex form (see Figure 8, a,b). As a rule, the indent has deformed borders and the whole picture often looks disordered. It is possible to create indents having a square-form without significant deformation (Figure 8c), but most indents are deformed and their boundary exhibit a complex non-linear shape. Due to the large number of indents, it is possible to classify this data.

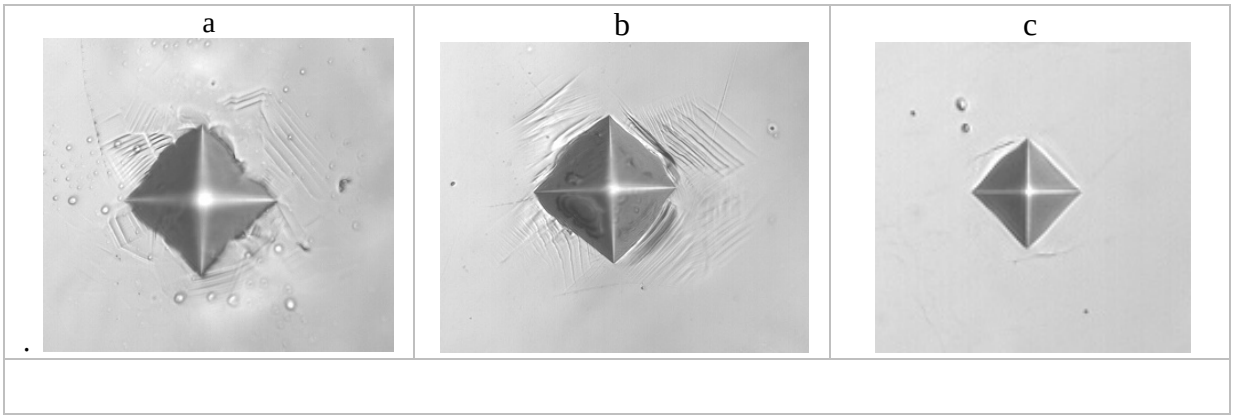

Figure 8: Examples of typical indenter indent geometry: a) HS-13 sample, 500 g load. b) ES-21, 500 g. c) BS-13, 100 g.

The material of this investigation has regular grain structure and the typical scale of grain size (10-40 microns) is comparable to the indent size (20-50 microns). This means that each indent's boundary interacts with one or more grains. Because deformation processes are sensitive to grain orientation, it is reasonable to expect to observe different pictures for each particular grain orientation.

For this analysis, it is easiest to start from indentations with the smallest (100 g) load because the indent border size (~20 microns) is comparable to the grain size. After analysis of ~50 indents it was found that all indent structures can be divided into 3 main categories:

- Clear-straight (or almost straight) borders without any deformation signs (or deformation signs are very light) (See Figure 9).
- Borders with a form-less shaft or heap of deformed material without deformation bands (See Figure 10).
- Clear linear-like structures similar to "hard-wood floor" relief (See Figure 11).

Certainly, these classifications aren't fully objective, containing a certain element of arbitrariness. There are images of borders, which can be classified to this or that type, or to allocate in separate "mixed" type. However, for this initial analysis, three categories were found to be sufficient.

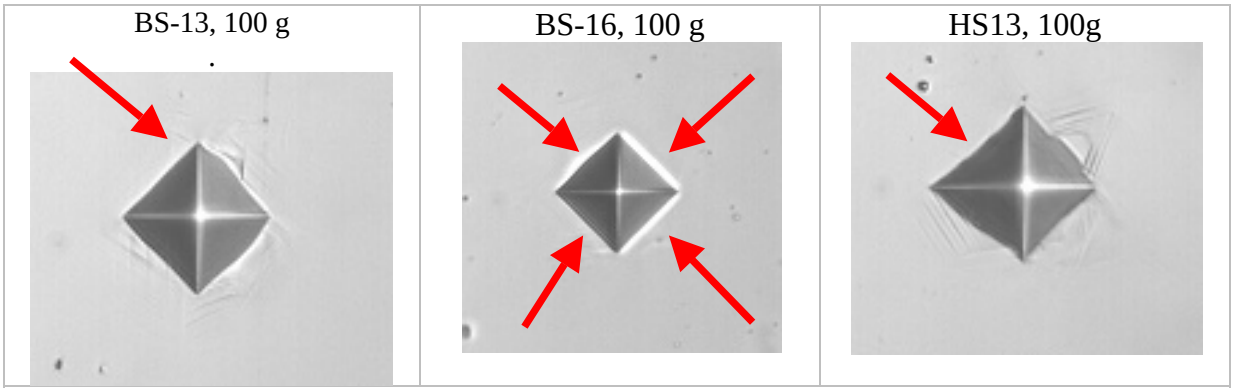

Figure 9: Clear borders of A-type (marked by arrows).

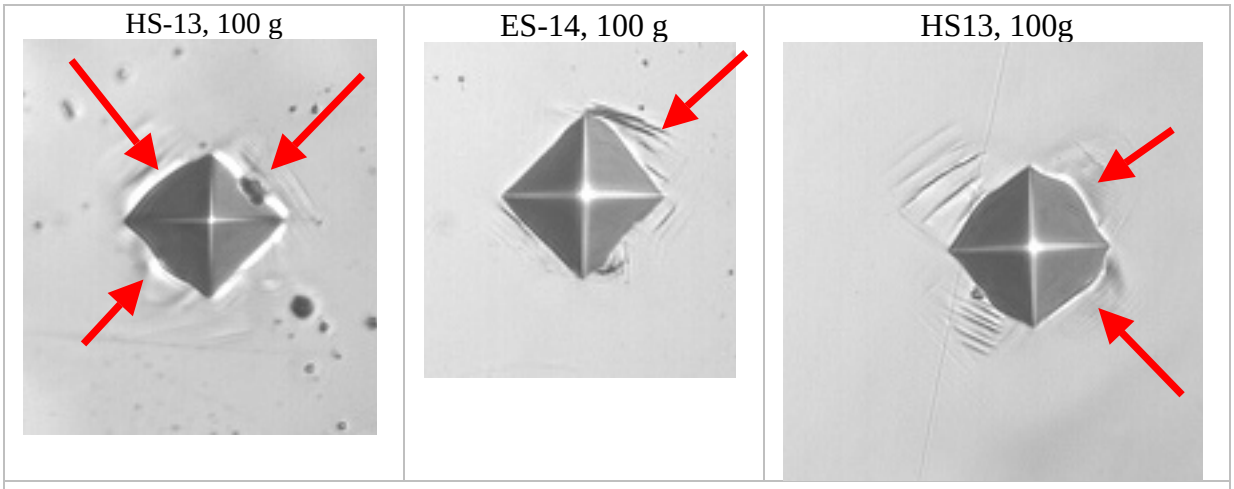

Figure 10: Borders of B-type (marked by arrows). One can see formless "hills" of material.

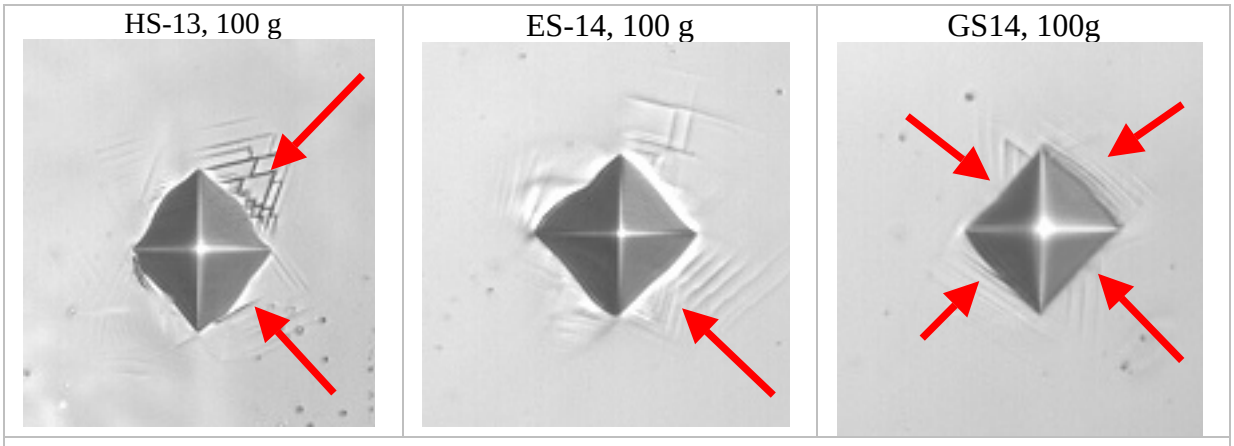

Figure 11: Borders of C-type (marked by arrows). It is possible to see deformation lines as "parquet-like" relief.

As shown on Figures 9-11, the low-load-indent boundary in most cases can be classified as single-type. The loading increase leads to a more complex picture. The border of the indentation now occupies some grains, and high load conducts to formation of complex, break boundary (See Figure 12).

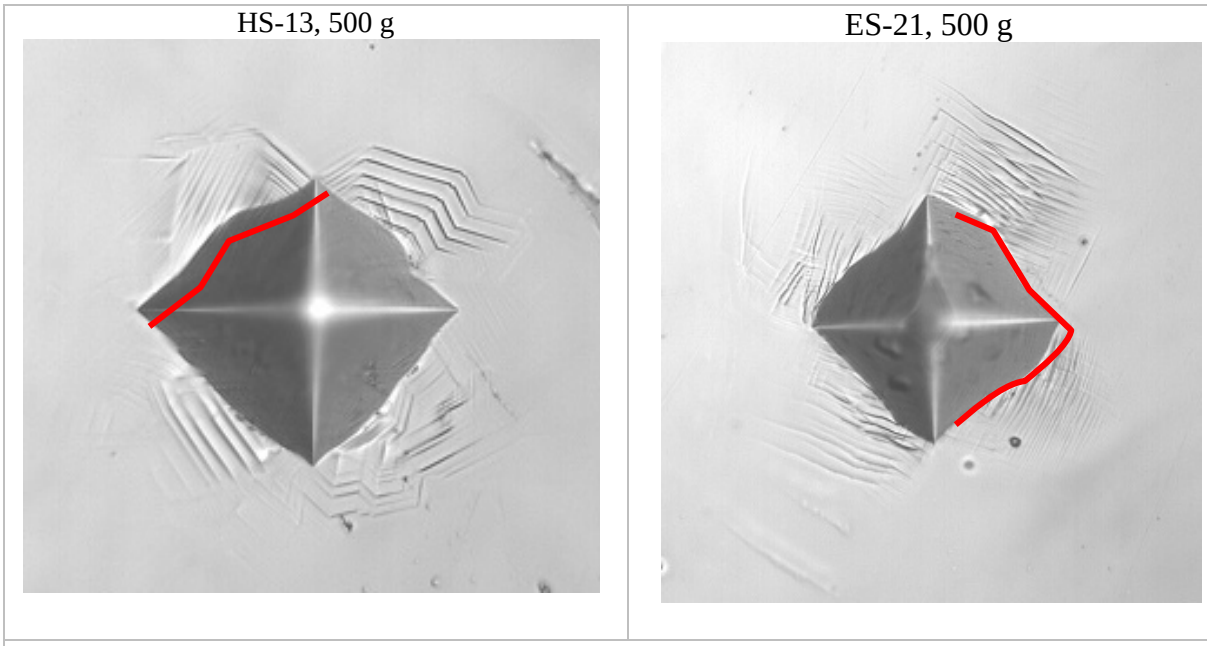

Figure 12: Examples of complex boundary. Most of the boundaries' perimeter is C-type boundary.

Usually complex shape boundaries for high-load indentations cannot be classified as single-type. In most cases it contains parts of different types (see Figure 13).

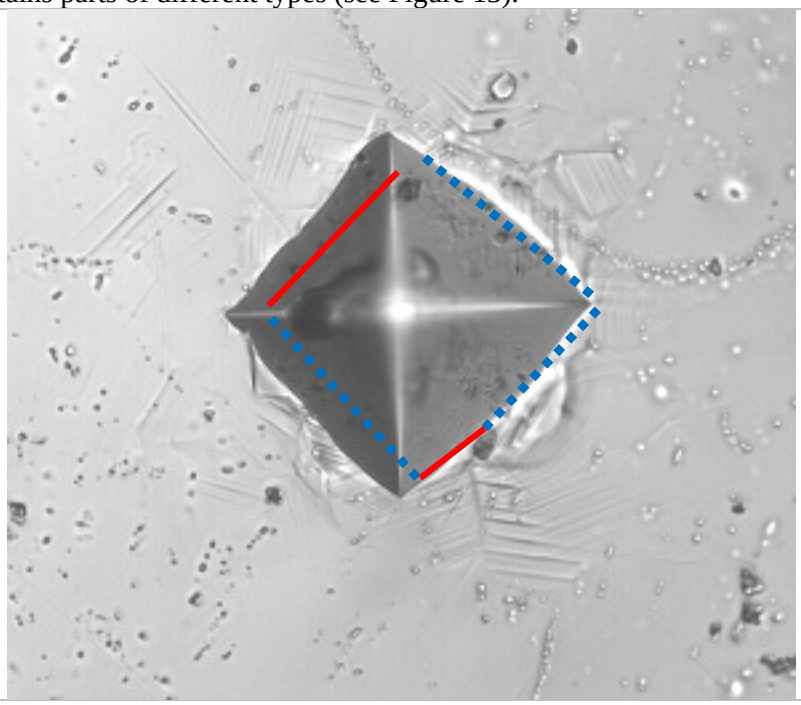

Figure 13: Examples of compels boundary with C (solid line) and B (dot line) parts. PS-15, 500g.

It is possible to assume, the near-boundary structure is connected to the material's deformation mechanisms. So, the structure we see is connected to material composition, structure and history. One can calculate the fractions of the perimeters related to different types of deformation and use this data to characterized the degree of localization (See table 7).

Table 7: Fraction of different stricture types (A,B,C) for different loads.

sample	load 100			load 200			load 500		
	A	**B**	**C**	**A**	**B**	**C**	**A**	**B**	**C**
BS16	**0.66**	**0.33**	**0**	**0.45**	**0.5**	**0.05**	**0.3**	**0.45**	**0.25**
BS13	**0.6**	**0.25**	**0.15**	**0.8**	**0.15**	**0.05**	**0.4**	**0.3**	**0.3**
PS15	0.55	0	0.45	0.25	0.05	0.7	0.05	0.25	0.7
ES21	0.4	0.4	0.2	0.1	0.2	0.7	0.02	0.16	0.82
HS13	0.4	0.25	0.35	0.15	0.05	0.8	0.1	0.15	0.75
B123	0.35	0.2	0.4	0.05	0.05	0.9	0.05	0.2	0.75
ES14	0.2	0.25	0.55	0.35	0.15	0.5	0.1	0.05	0.85
GS14	**0**	**0.05**	**0.95**	**0.1**	**0.1**	**0.8**	**0.03**	**0.03**	**0.94**

The data in Table 7 is sorted by fraction of A-structure for a 100 g load. That is, A-structure fraction volume (see column A for 100 g) decreases from BS16 to GS14 samples. With increasing load, the fraction of A-structure decreases and fraction of C-structure increases (up to ~100%). This rule has two major exceptions: BS-samples show a large amount of A-type boundaries for all loads, and – the GS14 sample almost always forms C-structure boundaries.

The tendency of dominant structure change can be illustrated also by the red diagonal arrow in Table 7: in general the part of C-type structure increases with increasing of load and from BS-samples to PS-15, ES-21 etc. One should also expect the influence of damage dose, although this question will be studied later in the program when more statistics are available.

The exceptions noted above (BS and PS), however, are very interesting and should be investigated in greater detail. As a working hypothesis, one may assume both these exceptions (BS-samples and GS14) are connected to unusual sample structures (small or very big grain size) and composition (exotic additions).

The general rule (increasing of C and decreasing of A with increasing load) for all other samples may be connected to the increasing volume of material deformed with the increasing indentation load. It is possible to assume the C-type structure is connected to the formation of defect-free channels and localized deformation. This phenomenon is well known for irradiated metal materials, and is expected to exhibit some critical volume. Further, the formation of defect-free channels system can be scale-sensitive. If one deforms a small portion of a grain, the defect free channels never forms, but if there are many grains under the indenter, the defect-free channels can form with a high probability.

5. DENSITY

Density and swelling measurements were performed using a procedure based on ASTM standard C135-96 [4]. The density measurements were performed on tensile specimens by an immersion density method. Non-irradiated control specimens were measured with the irradiated specimens for each material condition that was available. The density data from the irradiated specimens is compared with those of the control specimens, and void swelling quantified by the radiation-induced density changes. It is important to note that if significant precipitation occurs, the measured density change can be due to void swelling and/or phase change effects.

An immersion density method is widely used in determining the densities of specimens before and after irradiation. Immersion density measurements are based on the Archimedes' principle, and the density of a sample is calculated by its weight difference in air and in liquid. An immersion density measuring apparatus had been developed for previous ORNL programs [5]. The critical factors that affect the precision and accuracy of the measurements have been thoroughly analyzed and refined in the design of the instrument. The performance of the system was evaluated by measuring several high purity metals.

5.1 IMMERSION DENSITY PRINCIPLE

Immersion density measurements are based on the Archimedes' principle. The apparent weight reduction of an immersed body is equal to the mass of the displaced liquid. The density of a specimen can be determined by measuring its mass in air and its effective mass when submerged in a liquid with a known-density. The density of the specimen is calculated using the following equation:

$$\rho_{sample} = \frac{W_{sample}^{air} \times \rho_{fluid}(T)}{W_{sample}^{air} - W_{sample}^{fluid}} \qquad (1)$$

where ρ_{sample} is the density of the specimen, ρ_{fluid} (T) is the density of the liquid at the test temperature, T, W^{air}_{sample} is the mass of the specimen in air, and W^{fluid}_{sample} is the mass of the specimen in liquid.

The immersion density-measuring unit consists of an ultra-sensitive balance, the Satorius ME215S, a density kit, and a high-precision digital thermometer. The balance has a resolution of 0.010 mg and a reproducibility of ±0.015 mg in a weight range of 0–60 g. The digital thermometer has a resolution of 0.001°C with an accuracy of ±0.05°C. The density kit includes a beaker filled with a high-density fluid, a specimen holder, a thin wire (0.007 in. in diameter) for suspending the specimen holder in liquid, and a metal platform supporting the beaker. The entire density unit is set up on a marble table in a stable environment to minimize vibrations and temperature perturbations.

3M Fluorinert™ Liquid FC-43 was chosen as the preferred liquid due to its high density (nearly double that of water at room temperature). It also has low surface tension, low thermal expansion, low vapor pressure, and low water/air solubility, which are critical factors in measuring densities accurately. Since the liquid density is primarily affected by temperature variations, the temperature dependence of FC-43 density needs to be determined accurately. The density-temperature relation of FC-43 was derived from the data obtained by measuring National Institute of Standards and Technology (NIST) traceable marble standards of known densities (2.699, 2.900 and 3.200 g/cm^3). The density data were fitted using both a linear function and an exponential function. Figure 14 shows the calibrated density of FC-43 as a function of temperature. The exponential fitting gave a coefficient of 0.0012, which agrees with the thermal expansion coefficient of this fluid. The linear temperature dependence was employed for simplicity, and is given as:

$$\rho(g/cm^3) = 1.93511 - 0.00223 \times T\left(^oC\right) \quad (2)$$

All the density measurements are carried out at room temperature.

The general procedure for measuring the densities of refractory alloy specimens begins with zeroing the balance and weighing the specimen in air. A beaker is then filled with approximately 300 ml of the FC-43 solution. The beaker is placed on a metal platform that rests on the base of the weighing chamber and a specimen holder is suspended in the solution using a thin wire. After allowing the solution to stabilize for at least an hour, the specimen is placed in the solution and allowed to completely wet. The balance is then zeroed and the weight of the immersed specimen is recorded. The liquid density at the measuring temperature is determined by eq. (2).

The specimen densities are calculated using eq. (3) that accounts for air buoyancy (ρ_{air} = 0.0012 g/cm^3 at T = 20°C and P = 101.325 kPa), i.e.

$$\rho_{sample} = \frac{W_{sample}^{air} \times \left(\rho_{fluid}(T) - \rho_{air}\right)}{\left(W_{sample}^{air} - W_{sample}^{fluid}\right)} + \rho_{air} \quad (3)$$

A standard specimen is measured to calibrate the density-measuring unit before measuring test specimens. Each specimen is measured three times. If more than three measurements are made, the highest and lowest values are discarded and the average and standard derivation were calculated from the remaining three measurements.

Several high purity metals, Fe, Cu, Mo, Ag, and Pd, have been measured in past campaigns to evaluate the performance of the immersion density-measuring unit. The materials selected span a range of density between 8 and 21 g/cm^3. The results [5] indicate that the density measurements are both repeatable and accurate over a wide range of densities. The measured density for copper is lower than the published value from [6] for both sets of data.

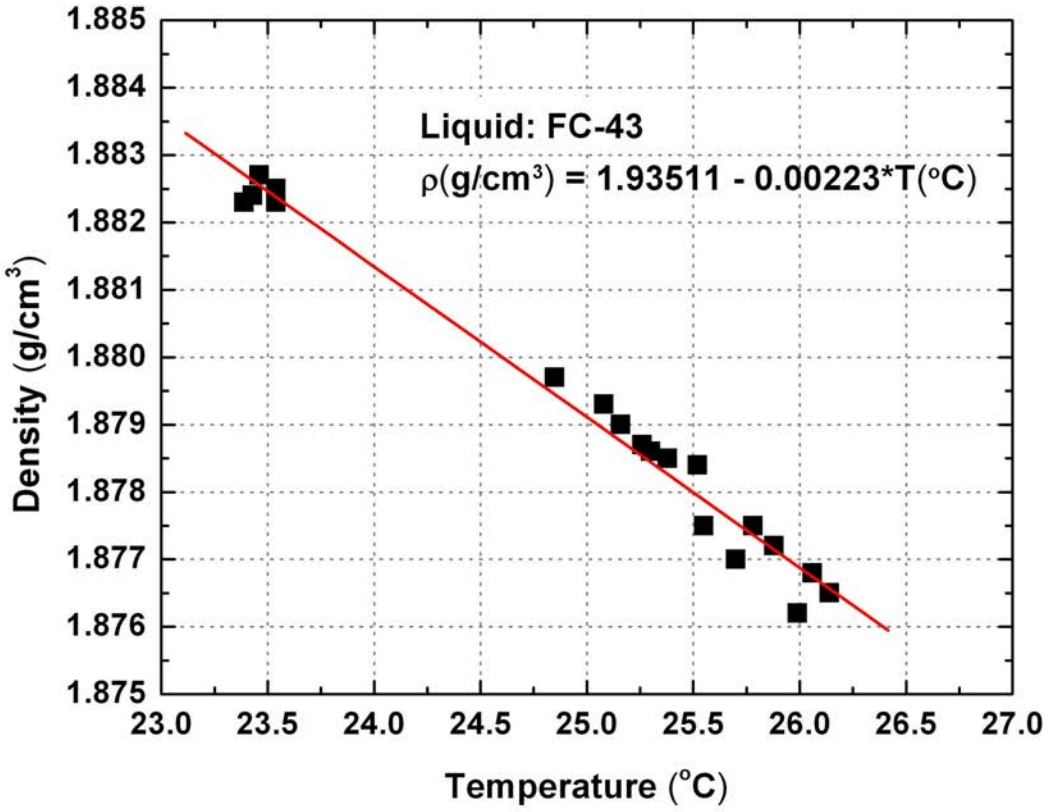

Figure 14: Temperature dependence of FC-43 density.

5.2. IMMERSION DENSITY RESULTS

For density measurements of this study, the procedure described above was used. Each sample was weighted 3 times in air and 3 times in liquid. The temperature was measured with accuracy not worse than 0.2°C before and after each sample measurement. The sample code, material, damage dose, and density values are given in Table 8 for all samples. Data on the samples' weight in water and in air are listed for reference.

Table 8: Density values for first set of BOR-60 samples

Sample code	Material	Dose, dpa	Average weight in air	Average weight in water	Density, g/cm^3	Swelling (%)
B123	CW316	25	2.25007	1.717163	7.954	0.58%
BS13	SA316	5.5	1.838767	1.402463	7.938	0.78%
BS16	SA316	10.2	1.828937	1.39475	7.934	0.82%
ES21	HP304	10.7	1.819207	1.388913	7.964	0.45%
ES14	HP304L	11.8	1.83001	1.39734	7.967	0.41%
HS13	HP304+Si	7.8	2.12617	1.618463	7.888	1.40%
PS15	HP304+Hf	9.6	2.149903	1.64641	8.043	-0.54%
GS14	HP304+Mo	11.8	1.857243	1.420707	8.013	-0.16%

It is possible to see from the table, density values for B123, BS13, and BS16 are relatively close to each other. Since the damage doses for all HP-samples (high purity 304 steel) are similar, one can compare density values and try to assess the role of alloying elements. There is no difference in the ES series of alloys. Addition of Si to HP304 steel (sample HS13) decreases the density after irradiation, but addition of Hf or Mo (samples PS15 and GS14 respectively) leads to increasing of density, although the difference for the GS alloy is likely within the uncertainty of the measurement. Densification is observed for the PS alloy. This may be due to the formation of Hf-rich phases under irradiation and more analysis is required.

6. SUMMARY

The Light Water Reactor Sustainability (LWRS) Program is designed to support the long-term operation (LTO) of existing domestic nuclear power generation with targeted collaborative research programs into areas beyond current short-term optimization opportunities. The Materials Aging and Degradation Pathway is designed to help develop the scientific basis for understanding and predicting long-term environmental degradation behavior of materials in nuclear power plants and to provide data and methods to assess performance of systems, structures, and components essential to safe and sustained operation.

Extended service conditions will increase the exposure to irradiation, stress, and corrosive environment for all core internal components. The effects of irradiation can substantially increase susceptibility to stress-corrosion cracking of austenitic steels in high-temperature water environments. IASCC is a key materials degradation issue in today's nuclear power reactor fleet and affects critical structural components within the reactor core. Despite 30 years of experience, the underlying mechanisms of IASCC are unknown. The objective of this work is to evaluate the response and mechanisms of IASCC in austenitic stainless steels with single variable experiments.

A series of high-value irradiated specimens has been acquired from the past CIR program, providing a valuable opportunity to examine the mechanisms of IASCC. This batch of irradiated specimens has been received and inventoried. In addition, visual examination and sample cleaning has been completed.

Microhardness testing has been performed on these specimens. All samples show evidence of hardening, as expected, although the degree of hardening has saturated and no trend with dose is observed. Further, the change in hardening can be converted to changes in mechanical properties. The calculated yield stress is consistent with previous data from light water reactor conditions.

In addition, some evidence of changes in deformation mode was identified via examination of the microhardness indents. This analysis may provide further insights into the deformation mode under larger scale tests.

Finally, swelling analysis was performed using immersion density methods. Most alloys showed some evidence of swelling, consistent with the expected trends for this class of alloy. The Hf-doped alloy showed densification rather than swelling. This observation may be related to the formation of second-phases under irradiation, although further examination is required.

7. REFERENCES

1. Light Water Reactor Sustainability Research Program Plan, INL Document, INL/MIS-08-14918 rev 3, September 2010.

2. G.S. Was, Y. Ashida, K. Stephenson, and P. Andresen, "Identifying Mechanisms and Mitigation Strategies for Irradiation Assisted Stress Corrosion Cracking of Austenitic Steels in LWR Core Components," University of Michigan Semi-annual report, Sept. 2010.

3. J.T. Busby, M.C. Hash, and G.S. Was, "The Relationship Between Hardness and Yield Stress in Irradiated Austenitic and Ferritic Steels," J. Nucl. Mater. Vol. **336**, 2-3 (2005), 267-278.

4. "Standard Test Method for True Specific Gravity of Refractory Materials by Water Immersion", ASTM Designation C135-96. ASTM Standards Online, American Society for Testing and Materials, Philadelphia, PA, 2003.

5. Meimei Li, "Final Report on Post Irradiation Density Measurements of Molybdenum Specimens from Phases I, II & III," ORNL report to Naval Reactors, 2004 via private communication.

6. CRC Handbook of Chemistry and Physics, 84th Ed. CRC Press, Boca Raton, FL, 2003-2004.

This page intentionally left blank

INTERNAL DISTRIBUTION

1. J. T. Busby
2. T. Rosseel
3. M. Gussev
4. D. Williams
5. S. Zinkle

EXTERNAL DISTRIBUTION

6. R. Szilard, Idaho National Laboratory, P.O. Box 1625, Idaho Falls, ID 83415-3860, (Ronaldo.Szilard@inl.gov)
7. P. Finck, Idaho National Laboratory, P.O. Box 1625, Idaho Falls, ID 83415-3860, (Phillip.Finck@inl.gov)
8. R. Reister, GTN Bldg, 1000 Independence Ave, S.W. Washington, DC 20585, (Richard.Reister@nuclear.energy.gov)